ELSEVIER

Contents lists available at ScienceDirect

Mechanics of Materials

journal homepage: www.elsevier.com/locate/mecmat



Editor invited article

Fluid convection driven by surface tension during free-surface frontal polymerization

Yuan Gao ^{a,b,c}, Justine E. Paul ^{b,d}, Manxin Chen ^{b,c}, Aarav Seth ^{b,d}, Qibang Liu ^{b,c}, Liu Hong ^e, Leonardo P. Chamorro ^e, Randy H. Ewoldt ^{b,e}, Nancy R. Sottos ^{b,d,*}, Philippe H. Geubelle ^{b,c}

- a State Key Laboratory of Digital Manufacturing Equipment and Technology, Huazhong University of Science and Technology, Wuhan, 430074, China
- b Beckman Institute for Advanced Science and Technology, University of Illinois, Urbana, 61801, IL, United States
- ^c Department of Aerospace Engineering, University of Illinois, Urbana, 61801, IL, United States
- d Department of Materials Science and Engineering, University of Illinois, Urbana, 61801, IL, United States
- e Department of Mechanical Science and Engineering, University of Illinois, Urbana, 61801, IL, United States

ARTICLE INFO

Keywords: Frontal polymerization Surface-tension-driven flow Reaction-diffusion-convection system Particle image velocimetry Thermo-chemical instability

ABSTRACT

Frontal polymerization (FP) is an efficient method to manufacture thermoset polymers and composites, and is usually modeled as a reaction–diffusion (RD) process. In this study, we investigate numerically and experimentally how fluid convection ahead of the propagating front can impact the reaction–diffusion balance in the free-surface FP of dicyclopentadiene (DCPD) and 5-ethylidene-2-norbornene (ENB). Multiphysics finite element analyses reveal how the velocity of the surface-tension-driven flow described by the dimensionless Marangoni number can be modulated by varying the processing temperature and the viscosity of the monomer resin. The surface-tension-driven fluid velocity exhibits two distinct regimes, which arise from the interplay and competition between thermal and chemical advection. The dispersion of the reaction heat by the Marangoni flow leads to a reduction in the velocity of the front. The presence of fluid convection during FP can lead to instabilities in the front propagation and generate reaction patterns, which can be adjusted by controlling the initial temperature and degree of cure. The numerical findings are corroborated by experiments that combine FP and particle image velocimetry (PIV).

1. Introduction

Frontal polymerization (FP) involves a self-propagating polymerization front that transforms a monomer into a polymer, sustained by the enthalpy of the exothermic reaction (Chechilo et al., 1972; Pojman et al., 1996; Chen et al., 2006; Nason et al., 2005; Ruiu et al., 2014; Nuvoli et al., 2015; Washington and Steinbock, 2001; Suslick et al., 2023; Mariani et al., 2001), and has been reported as a timeand energy-efficient manufacturing method for thermoset polymers and composites (Robertson et al., 2018; Li et al., 2022). In most previous studies dedicated to modeling of FP, the initiation and propagation of the polymerization front are modeled as a reaction-diffusion (RD) process (Goli et al., 2018; Vyas et al., 2020; Aw et al., 2022). Several chemical and thermal factors play a critical role in the RD process, including the cure kinetics (Mariani et al., 2004; Ivanoff et al., 2020) and the pre-cure state (Goli et al., 2018) of the resin, the concentration of catalyst and inhibitor (Chen et al., 2006; Robertson et al., 2016; Suslick et al., 2021), the process temperature (Aw et al., 2022; Chen

et al., 2022), the heat loss to the surrounding (Tiani et al., 2022; Gao et al., 2022b), and the presence of a thermally conductive or heat-absorbing phase (Vyas et al., 2019; Gao et al., 2022a; Wang, 2022). These factors directly influence the temperature, velocity, and stability of the polymerization front (Kumar et al., 2021; Gao et al., 2021). Recently, a three-dimensional model for frontal polymerization of fiber-reinforced composites has been proposed and reveals that the front velocity depends on the triggering direction (Tarafdar et al., 2023).

When the monomer is in the liquid phase prior, the sharp thermal and chemical gradients in the vicinity of the polymerization front may trigger fluid convection across the front for liquid products (Belk et al., 2003; McCaughey et al., 1998) and in the uncured monomer in the case of solid products (Gao et al., 2023). Similar to reaction–diffusion-convection (RDC) processes in inorganic autocatalytic systems (Tiani et al., 2018; Mukherjee and Paul, 2022; Pojman, 2019; Bigaj et al., 2023; Liu et al., 2017), the presence of fluid convection during FP can affect the propagation of the front through the advection of heat and

Invited Editor: Ghatu Subhash.

^{*} Corresponding author at: Beckman Institute for Advanced Science and Technology, University of Illinois, Urbana, 61801, IL, United States. E-mail addresses: n-sottos@illinois.edu (N.R. Sottos), geubelle@illinois.edu (P.H. Geubelle).

chemical concentrations (Daytvan et al., 2011). When the fluid convection is induced by thermal-gradient buoyancy effects, the velocity and shape of the front become sensitive to the viscosity of the monomer resin (Bowden et al., 1997; Matthiessen et al., 1996) and the direction of the FP relative to gravity (Bazile et al., 2002). Convection-induced front instabilities have been observed with a governing bifurcation parameter, known as the frontal Rayleigh number (Garbey et al., 1996). In addition to the buoyancy effects, the presence of surface tension gradients at the liquid-air interface, resulting from variations in thermal and chemical properties, has the potential to induce fluid convection, specifically Marangoni flow, which has been identified as significant in submillimeter RDC systems (Bába et al., 2018). When FP occurs in an open mold, significant Marangoni flow can develop at the free surface of the monomer resin, resulting in the formation of material patterns and the potential emergence of heterogeneous properties in the polymer product (Lloyd et al., 2021). Understanding and characterizing the impact of Marangoni flow in open-mold FP is thus important to maintain the quality of the product as well as the design of surface patterns in the resulting polymeric parts.

In this study, we present a comprehensive investigation of Marangoniinduced convection during the FP of dicyclopentadiene (DCPD), employing both numerical simulations and experiments. In the case of FP in DCPD, multiphysics finite element analyses suggest that the velocity of the Marangoni convection is two orders of magnitude higher than the buoyancy-induced convection and has a substantial impact on the front shape. Governed by the Marangoni number derived from the dimensionless form of the RDC equations with free surface boundary condition, the Marangoni flow exhibits sensitivity to both the initial temperature and pre-cure state of the monomer resin. By varying the Marangoni number, two distinct regimes of fluid convection are observed, which can be attributed to the competition that arises between thermal and chemical advection of the Marangoni flow. The presence of fluid convection during FP disperses some of the heat released by the exothermic reaction, resulting in reduced front velocities compared to a convection-less system. Moreover, the presence of convective effects can contribute to the emergence of reaction patterns that are not present in the reaction-diffusion (RD) system. The numerical results are substantiated by FP experiments on the surface and convection flows using particle image velocimetry (PIV).

2. Computational methods

In this work, FP in a low-viscosity liquid resin such as DCPD and the associated fluid convection were modeled by coupling the reaction—diffusion partial differential equations (PDEs) with the incompressible Navier–Stokes equation under the Boussinesq approximation as (Belk et al., 2003)

$$\begin{cases} \rho C_{p} \left(\frac{\partial T}{\partial t} + \boldsymbol{u} \cdot \nabla T \right) = \kappa \nabla^{2} T + \rho H_{r} \left(\frac{\partial \alpha}{\partial t} + \boldsymbol{u} \cdot \nabla \alpha \right), \\ \frac{\partial \alpha}{\partial t} + \boldsymbol{u} \cdot \nabla \alpha = A \exp \left(-\frac{E}{RT} \right) (1 - \alpha)^{n}, \\ \nabla \cdot \boldsymbol{u} = 0, \\ \frac{\partial \boldsymbol{u}}{\partial t} + \boldsymbol{u} \cdot \nabla \boldsymbol{u} = -\frac{1}{\rho} \nabla p + \nabla \cdot \left[v(\alpha) (\nabla \boldsymbol{u} + (\nabla \boldsymbol{u})^{T}) \right] - \rho \boldsymbol{g}(T - T_{0}). \end{cases}$$
(1)

To make the equations complete, the variation of the kinematic viscosity $v(\alpha) = \mu(\alpha)/\rho$ (m² s⁻¹) as a function of the degree of cure was measured (see Section 3.5) and implemented by quadratic extrapolation in the numerical analysis (Fig. S1 in the Supplementary Material). μ (Pa s) is the dynamic viscosity, and ρ (kg m⁻³) denotes the density. These equations were solved over a two-dimensional (2-D) rectangular domain of length l=40 mm (in the x-direction) and height h=8 mm (in the y-direction) (Fig. 1). A length of 40 mm is sufficient for the front to reach a quasi-steady state, allowing data on the front motion and the associated fluid field to be collected. The selected height of 8 mm avoids interference between the fluid field and the bottom boundary along which a no-slip condition is applied for the

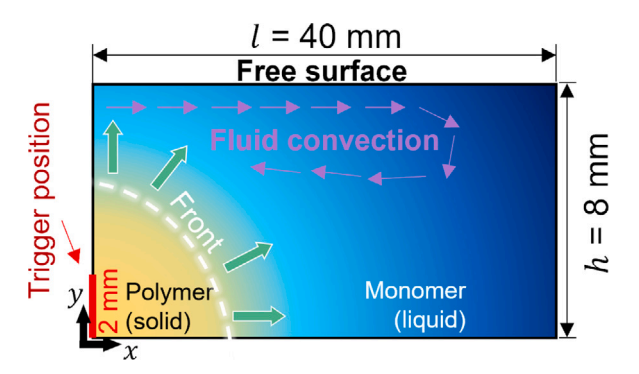


Fig. 1. Numerical domain for the simulation of the FP of DCPD in a system with a free surface.

fluid flow. The four variables of interest are the temperature T(x,y,t) (K), degree of cure $\alpha(x,y,t)$ (dimensionless), pressure p(x,y,t) (Pa), and fluid velocity vector $\mathbf{u}=(u_x(x,y,t),u_y(x,y,t))$ (m/s), with (x,y) and t denoting the spatial coordinates and time, respectively. The degree of cure α varies between 0 (monomer) and 1 (polymer) and describes the fractional conversion according to the enthalpy of the reaction. In the first equation, κ (W m⁻¹ K⁻¹), C_p (J kg⁻¹ K⁻¹), ρ (kg m⁻³), and H_r (J kg⁻¹) respectively represent the thermal conductivity, heat capacity, density, and heat of reaction of the DCPD resin. The thermal properties were assumed as constant during FP. The second relationship describes the cure kinetics model, where A (s⁻¹), E (J mol⁻¹), and R (= 8.314 J mol⁻¹ K⁻¹) respectively denote the pre-exponential factor, the activation energy, and the ideal gas constant. The molecular diffusion was neglected in the model.

The third and fourth relations correspond to the conservation of mass and momentum, respectively. The last term describes the fluid flow driven by the buoyancy effect, where β (K⁻¹) and g (0, -9.81 N kg⁻¹) are the thermal expansion coefficient and the gravitational body force vector acting in the negative y-direction. The thermal expansion coefficient of slightly cured DCPD was 5×10^{-4} K⁻¹ (Kumar et al., 2024; Koohbor et al., 2023). In the present study, we assumed that the β of liquid monomer DCPD is slightly higher, 6×10^{-4} K⁻¹, and remains constant in the simulations. As α increases from 0 to 1, the viscosity grows by \sim 6 orders of magnitude according to the experimental measurement. The polymerized resin is considered a liquid with a very high viscosity.

The governing equations (1) were solved with the following initial and boundary conditions:

$$\begin{cases}
T(x, y, 0) = T_0, & 0 \le x \le l, & 0 \le y \le h, \\
\alpha(x, y, 0) = \alpha_0, & 0 \le x \le l, & 0 \le y \le h, \\
T(0, y, t) = T_{\text{trig}}, & 0 \le y \le \frac{1}{4}h, & 0 \le t \le t_{\text{trig}}, \\
\frac{\partial T}{\partial x}(0, y, t) = 0, & 0 \le y \le \frac{1}{4}h, & t > t_{\text{trig}}, \\
\frac{\partial u_x}{\partial y}(x, h, t) = -\frac{1}{\nu\rho}\frac{\partial \gamma}{\partial x}, & 0 \le x \le l,
\end{cases}$$
(2)

where T_0 (20 °C), α_0 (0.01), T_{trig} (200 °C), and t_{trig} (5 s) are the initial temperature and degree of cure, triggering temperature, and triggering time, respectively. A Dirichlet thermal boundary condition was applied along the bottom quarter of the left boundary to trigger the front and was replaced by an adiabatic boundary after t_{trig} . Adiabatic boundary conditions were applied along the top, bottom, and right boundaries. The last expression corresponds to the Marangoni condition, where u_x and γ denote the x-component of the surface velocity vector and the surface tension, respectively. Only thermal effects on surface tension were considered given that the effect of the degree of cure α was captured in the kinematic viscosity. Therefore, $\frac{\partial \gamma}{\partial x} = \frac{\partial \gamma}{\partial T} \frac{\partial T}{\partial x}$, with the thermal capillary coefficient $\frac{\partial \gamma}{\partial T} = -2.2 \times 10^{-4}$ N m⁻¹ K⁻¹ measured experimentally (Fig. S2 in the Supplementary Material). No-slip boundary conditions were applied along the bottom, left, and right boundaries.

Table 1
Thermal properties of resin layer and substrate materials

κ (W m ⁻¹ K ⁻¹)	ρ (kg m ⁻³)	C_p (J kg ⁻¹ K ⁻¹)	$D = \kappa/(\rho \cdot C_p)$ $(m^2 s^{-1})$	β (K ⁻¹)
0.15	980	1 600	9.57×10^{-8}	6×10^{-4}

Table 2
Cure kinetic parameters of DCPD

A (s ⁻¹)	E (J mol ⁻¹)	n	$H_{\rm r}$ (J kg ⁻¹)
1.54×10^{12}	92 800	2.3	360 000

The Multiphysics Object-Oriented Simulation Environment (MOOSE) (Gaston et al., 2009), an open source C++ finite element solver with robust mesh and time-step adaptivity was used to capture the sharp gradients in temperature, degree of cure, and fluid velocity in the vicinity of the advancing polymerization front while handling the significant variation in the viscous property. The initial mesh size was 0.1 mm, and an h-level of 4 was adopted for the mesh adaptivity. The initial timestep was set as 10^{-4} s with time step adaptivity reducing this initial value by a factor 4. The material properties and cure kinetics parameters used in the numerical study are given in Tables 1 and 2. All parameters were adopted from a previous study (Gao et al., 2023).

The non-dimensional form of the governing equations (1) is

$$\begin{cases} \frac{\partial T^*}{\partial t^*} + \mathbf{u}^* \cdot \nabla^* T^* = \nabla^{*2} T^* + \left(\frac{\partial \alpha}{\partial t^*} + \mathbf{u}^* \cdot \nabla^* \alpha\right) \left(\frac{1}{1 - \alpha_0}\right), \\ \frac{\partial \alpha}{\partial t^*} + \mathbf{u}^* \cdot \nabla^* \alpha = Z \exp\left[\frac{\delta (T^* - 1)}{T^* + \varphi}\right] (1 - \alpha)^n, \\ \nabla^* \cdot \mathbf{u}^* = 0, \\ \frac{\partial \mathbf{u}^*}{\partial t} + \mathbf{u}^* \cdot \nabla^* \mathbf{u}^* = -\nabla^* p^* + \nabla^* \cdot \left[\Pr(\nabla^* \mathbf{u}^* + (\nabla^* \mathbf{u}^*)^{\mathrm{T}})\right] - \Pr\mathrm{Ra} T^* \hat{\mathbf{g}}, \end{cases}$$

$$(3)$$

where all superscripts '*' indicate variables or operators normalized by the characteristic time $t_c = D/v_c^2$, length $l_c = D/v_c$, pressure $p_c = v_c^2 \rho$, and velocity $v_c = [\frac{A\kappa RT_f^2}{\rho H_r(1-\alpha_0)E} \exp(-\frac{E}{RT_f})]^{0.5}$. The nondimensional temperature $T^* = (T-T_0)/(T_f-T_0)$, where $T_f = T_0 + H_r(1-T_0)$ $\alpha_0)/C_p$ is the adiabatic front temperature. The unit vector $\hat{\mathbf{g}}=(0,-1)$ 1) denotes the orientation of the gravity and $D = (\kappa/\rho C_n)$ is the thermal diffusivity. The characteristic velocity v_c is proportional to the steady-state front velocity v_f (Kumar et al., 2021). In the second relationship, $Z = H_r(1 - \alpha_0)E/(C_pRT_f^2)$ is the Zeldovich number, while the dimensionless parameters $\delta = E/(RT_f)$ and $\varphi = T_0/(T_f - T_0)$ capture the contributions of the activation energy and the processing condition. Although A appears in the dimensional equations, it disappears in the dimensionless equations and does not even appear in the parameter Z, as it cancels out due to the definition of the normalizing velocity, which is proportional to A. In the fourth equation, Pr = v/D is the Prandtl number, and Ra = $\beta |\mathbf{g}| (T_f - T_0) D^2 / (v v_c^3)$ is the frontal Rayleigh number that compares the buoyancy and front propagation. The derivation of the non-dimensional governing equations can be found in the Appendix S1 of the Supplementary Material.

The Marangoni boundary condition can be normalized as

$$\frac{\partial u_{X}^{*}}{\partial y^{*}} = \operatorname{Ma} \frac{\partial T^{*}}{\partial x^{*}},\tag{4}$$

where the Marangoni number

$$Ma = -\frac{(T_f - T_0)}{v_c \mu} \frac{\partial \gamma}{\partial T}$$
 (5)

is the key parameter that governs the convection driven by the surface tension effect. Ma is a function of the initial degree of cure (α_0) and temperature (T_0) of the monomer resin, as highlighted in Fig. 2. A higher α_0 results in an elevated viscosity and lower $T_{\rm f}$, which limits the fluid convection and corresponds to a lower Ma. An increased T_0

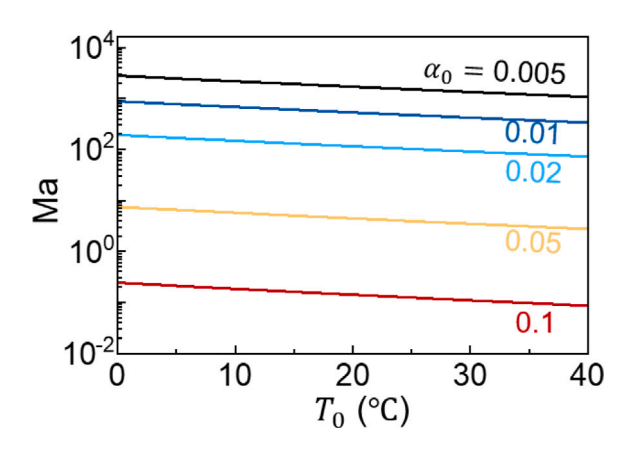


Fig. 2. Marangoni number Ma as functions of the initial temperature T_0 and degree of cure α_0 .

promotes an increase in the characteristic velocity $v_{\rm c}$, which also leads to a lower Ma.

To highlight the effect of fluid convection on the front propagation, the FP process was also modeled hereafter in the absence of fluid convection using the traditional thermo-chemical model as

$$\begin{cases} \rho C_p \frac{\partial T}{\partial t} = \kappa \nabla^2 T + \rho H_r \frac{\partial \alpha}{\partial t}, \\ \frac{\partial \alpha}{\partial t} = A \exp(-\frac{E}{RT})(1 - \alpha)^n, \end{cases}$$
 (6)

combined with the first four boundary and initial conditions in (2) and adiabatic boundary conditions along the other boundaries.

3. Materials and experimental methods

3.1. Materials

The materials involved in the experiments were dicyclopentadiene, 5-ethylidene-2-norbornene (ENB), and Grubbs' second-generation catalyst (GC2) purchased from Sigma-Aldrich, and tributyl phosphite inhibitor (TBP) purchased from TCI Chemicals. All chemicals were used as received without further purification. The rectilinear mold was fabricated with 1 mm thick glass slides (3" \times 1") and 1" flash tape purchased from Fiber Glast. The resistive heating wire used to trigger frontal polymerization in the free-surface geometry was a 26-gauge Kanthal wire (diameter 0.40 mm; resistivity $1.4\times10^{-4}~\Omega$ cm).

3.2. Resin preparation

To prepare the monomer resin for FP, a stock solution of 70 wt% DCPD, which is a solid at room temperature, and 30 wt% ENB were mixed in a 500 mL clear glass storage bottle. The addition of ENB allows for the monomer resin to stay a liquid at room temperature. The monomer solution was then degassed for about 2 h at room temperature under vacuum at -25 mmHg while being stirred. The monomer resin formulation for experiments was composed of 15 mL of the 70:30 DCPD:ENB solution. This solution was added to a 20 mL scintillation vial, and 3.07 μL (1 molar equivalent with respect to GC2) of tributyl phosphite (P(OBu)₃) inhibitor was added using a microliter syringe. 9.63 mg of GC2 (100 ppm) and 0.2 mg of 10-µm-diameter hollow silver spheres were then added to the monomer resin and sonicated for 5 min to achieve complete dissolution of the catalyst. Next, the monomer resin was either immediately transferred into the rectilinear open molds or placed in an environmental chamber at 25 °C for a set amount of time to achieve a higher degree of cure prior to conducting the FP experiments.

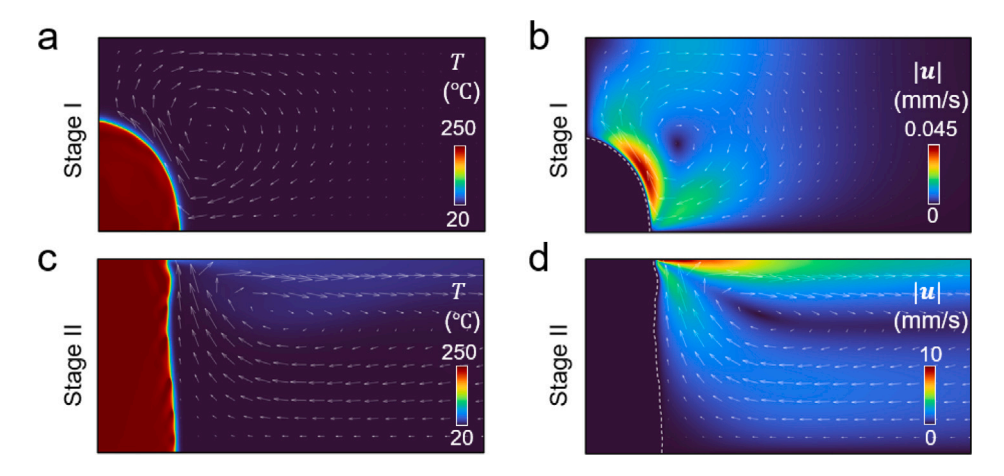


Fig. 3. Numerical snapshots of (a), (b) the temperature T and (c), (d) the magnitude of fluid velocity vector |u| on the two stages of FP.

3.3. Frontal polymerization and flow field measurements

The FP experiments were carried out in a rectilinear (7.5 cm \times 2.5 cm) free-surface geometry. The volume of resin in each sample was fixed at 15 mL so that the height of the free surface is ~8 mm, consistent with simulations. The polymerization is triggered using a 26-gauge resistive wire and an Agilent (U8031 A) triple output programmable DC power supply (3.5 V, 3.0 A, 5 s). The initial resin temperature and the ambient temperature were maintained in a custom-built environmental chamber equipped with an AC-162 Peltier module, TC-720 temperature controller, and PS-2425 power supply from TE Technology, Inc. The target initial temperature T_0 was achieved by setting the environmental chamber to the desired temperature and monitoring with a thermocouple. Flow field measurements were acquired within a specified region using particle image velocimetry with a DSLR Canon EOS R5 camera. It was positioned on the side of the closed mold system and directed towards the region of interest, observable through a polycarbonate window integrated into the environmental chamber. The medium under investigation was illuminated in a vertical plane along the x-direction using a 532 nm laser. Representative optical snapshots of the frontal polymerization are presented in Fig. S3 in the Supplementary Material.

3.4. Heat of reaction of the monomer resin

The cure kinetic of the liquid resin was extracted from differential scanning calorimetry (DSC) measurements performed with a TA Instruments Q250 differential scanning calorimeter. In these tests, samples were transferred into aluminum hermetic DSC pans at room temperature and sealed. The sample mass was determined using an analytical balance (XPE205, Mettler-Toledo) and was carefully maintained between 1 and 3 mg to achieve a maximum heat flow between 6 and 10 mW. Samples were subjected to thermal scans from -20 to $250~^{\circ}\text{C}$ at a constant ramp rate of 7 $^{\circ}\text{C}$ min $^{-1}$ to determine the cure kinetics of the monomer resin used in experiments. The heat released during the polymerization was then calculated by integrating the exotherm peak. Two typical DSC curves of DCPD resin with different pre-gelling states are given in Fig. S4 in the Supplementary Material.

3.5. Viscosity measurements of the monomer resin

The viscosity of the monomer resin at various times of incubation at 25 °C were measured in the TA Instruments DHR-3 rheometer equipped with a 25-mm-diameter flat plate, Peltier plate, and a solvent trap cover. Approximately 0.5 mL of resin was placed between the 25-mm-diameter flat plate and Peltier plate. A loading gap of ca. 950 μm was used for each test. The rheometer was set to 25 °C and a flow peak hold test with a constant shear rate of 10 s $^{-1}$ over time (180 s) was

performed to calculate the viscosity of the resin prior to conducting experiments. The viscosity was averaged between 30 and 180 s, with a sampling interval of 30 s/pt.

3.6. Methods for controlling initial degree of cure

The degree of cure, α_0 , was set by letting the monomer resin sit at 25 °C in an environmental test chamber (MicroClimate, Cincinnati Sub-Zero Products) for a specific amount of time to allow the resin mixture to increase in viscosity. DSC was then used to measure the enthalpy of reaction at various time points of the resin incubation, $H_{\rm res}(t)$ and the degree of cure was determined by

$$\alpha_0 = 1 - \frac{H_{\text{res}}(t)}{H_{\text{r}}},\tag{7}$$

where $H_{\rm r}$ was measured at t=0 min resin, i.e., immediately after preparing the resin.

4. Results and discussion

4.1. Typical numerical solution

A typical solution to Eqs. (1) and (2) with $T_0 = 20$ °C and $\alpha_0 = 0.01$ is presented in Fig. 3. As mentioned earlier, the front is triggered from the bottom left of the system using the bottom quarter of the left boundary, as described by (2)3,4. The front propagation is characterized by two stages based on the two different types of fluid convection (Rayleigh and Marangoni). Before the front reaches the top free surface, the fluid convection is induced solely by the buoyancy effect (Stage I). Representative distributions of the temperature T and fluid velocity magnitude |u| are shown in Fig. 3a, b, where the arrows indicate a fluid vortex in the clockwise direction ahead of the propagating front. The dashed lines correspond to the instantaneous position of the front identified hereafter by $\alpha = 0.5$. The largest magnitude of the fluid velocity is located just ahead of the front, where the temperature variation $T - T_0$ is maximized by the enthalpy of the reaction H_r . As a result of the substantial viscosity increase in the polymerized region, the velocity field rapidly vanishes.

Once the front approaches the free surface, the thermal gradient of the front drives the surface tension gradient, leading to a Marangoni flow whose magnitude exceeds that of the buoyancy-driven convection by more than two orders of magnitude (Stage II, Fig. 3c, d). This observation suggests that the fluid convection is primarily governed by the surface tension effect throughout the remainder of the FP process. The substantial fluid momentum, coupled with thermal and chemical advection, gives rise to instabilities that are evident through localized thermal spikes and irregularities ("kinks") in the front shape. These phenomena are further discussed later. For a visual representation, Video S1 in the Supplementary Material showcases an animation depicting a typical numerical solution.

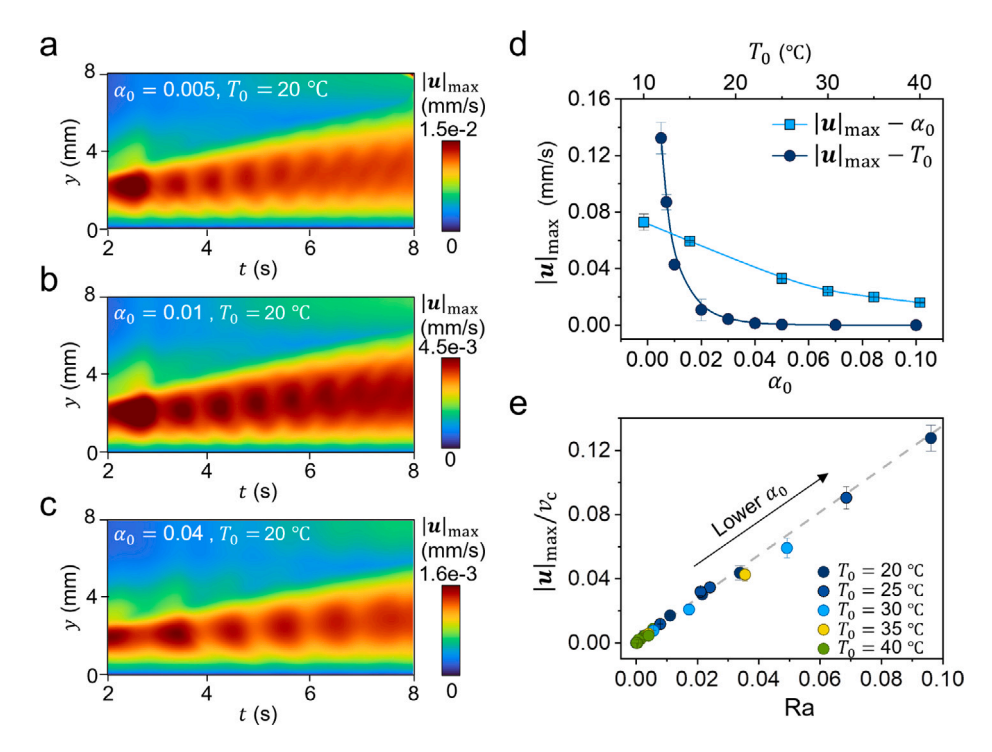


Fig. 4. Buoyancy-induced convection in Stage I. (a)–(c) Temporal variation of the maximum fluid velocity vector magnitude $|u|_{\text{max}}$ distributed on the *y*-axis obtained for initial degree of cure $a_0 = 0.005$, 0.01, and 0.04. (d) $|u|_{\text{max}}$ as functions of the initial temperature T_0 and degree of cure a_0 . (e) Normalized fluid velocity magnitude $|u|_{\text{max}}/v_c$ as a function of the frontal Rayleigh number Ra.

4.2. Buoyancy-induced convection ahead of polymerization front

Stage I of the FP process typically spans the initial 8 s until the front reaches the free surface. The temporal variation of the maximum fluid velocity magnitude $|u|_{\rm max}$ distributed on the *y*-axis (vertical) is shown in Fig. 4a-c. The fluid velocity remains zero at y=0 as enforced by the non-slip boundary condition. The fluid field expands in the *y*-direction as the front propagates to the top right of the domain. The convection triggers spin-mode instabilities indicated by the oscillations in $|u|_{\rm max}$ and the heterogeneous distribution of maximum reaction rates (Fig. S5 in the Supplementary Material). As the initial degree of cure a_0 increases, the oscillation period is extended due to a slower front velocity.

Fig. 4d indicates that $|\mathbf{u}|_{\text{max}}$ is suppressed by larger values of α_0 (squares) and T_0 (circles). The values of $|\mathbf{u}|_{\text{max}}$ are determined by taking the time average of the maximum value over the 4-8 s time interval. The reduction of the fluid velocity with α_0 is associated with the substantial increase in the viscosity of the resin. As T_0 increases, the front velocity $v_{\rm f}$ increases and the curing process occurs more rapidly, leading to a more rapid increase in the resin viscosity, which in turn limits the fluid convection. As shown in Fig. 4e, the effects of T_0 and σ_0 on the fluid velocity normalized by the characteristic velocity $|\mathbf{u}|_{\rm max}/v_{\rm c}$ can be combined in the form of a linear scaling law expressed as a function of the frontal Rayleigh number Ra introduced in Eq. (3).

4.3. Marangoni convection in FP

When the polymerization front reaches the free surface (top boundary), the thermal gradient induces a surface-tension gradient, initiating Marangoni convection (Stage II). Numerical snapshots of T^* and |u| are presented in Fig. 5. At t=10 s, a thermal spike emerges as the front reaches the free surface (Fig. 5a) due to the adiabatic condition applied along the top boundary of the domain. The associated temperature (normalized by the steady-state front temperature) reaches $T^* \sim 1.3$. The inset displays the distribution of the degree of cure α near the propagating front. According to the Marangoni boundary condition in

Eq. (4), the pronounced thermal gradient caused by the thermal spike leads to a substantial increase in fluid velocity orders of magnitude larger than the propagation front, as illustrated in Fig. 5b.

At t=20 s, the front location at the top boundary catches up with that at the bottom boundary and the front becomes nearly vertical. In the temperature distribution (Fig. 5c), a warmer region emerges ahead of the front near the free surface as the fluid convection disperses part of the reaction heat ahead of the polymerization front. Fig. 5d presents a snapshot of the quasi-steady-state fluid solution. As indicated in Fig. S6 in the Supplementary Material, the fluid velocity oscillates around a stable value in the quasi-steady-state regime. It is important to note that the maximum fluid velocity in the immediate vicinity of the free surface is an order of magnitude higher than the front velocity, and the resulting strong momentum generates a circulation pattern that expands throughout the numerical domain.

The clockwise fluid convection transfers reaction heat from the bottom to the top of the system. As the front speed increases with the temperature of the resin, the front velocity at the free surface is higher than along the bottom boundary, gradually leading to the front profile at t=35 s (Fig. 5e). As the front propagates closer to the right boundary of the computational domain, the fluid velocity is increasingly suppressed. This observation is further supported by the temporal variation of the maximum fluid velocity displayed in Fig. S6.

Next, a parametric study is carried out to investigate the effects on the Marangoni convective flow of the FP process conditions, i.e., the initial degree of cure α_0 and the initial temperature T_0 . Fig. 6a-c presents the spatial distribution of the fluid velocity magnitude |u| at t=20 s for three α_0 values: 0.005, 0.008, and 0.015. Interestingly, |u| is enhanced as α_0 grows from 0.005 to 0.008 but then decreases for $\alpha_0=0.015$, indicating a non-monotonic trend. Furthermore, for the larger value of α_0 , the spatial extent of the convective vortex ahead of the front reduces as the fluid velocity decreases due to the higher initial viscosity of the resin. As shown in Fig. 6d-f, which present the fluid solution at t=20 s for three T_0 values: 30, 40, and 45 °C, the strength of the convective vortex decreases as T_0 increases due to the faster curing process taking place at higher temperature.

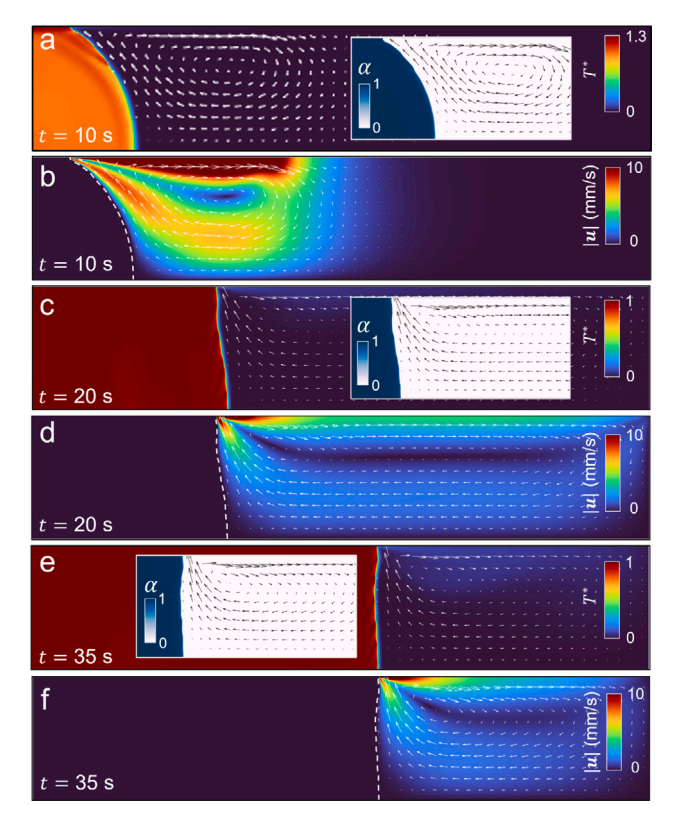


Fig. 5. Marangoni convection during free-surface FP. (a),(c),(e) Snapshots of the normalized temperature T^* during the FP on Stage II when the time t=10, 20, and 30 s. Inset: corresponding distributions of the degree of cure α . (b),(d),(f) Snapshots of the fluid velocity magnitude |u| at t=10, 20, and 30 s. The arrows indicate the orientation of local velocity vectors and the dashed lines correspond to the position of the front for which $\alpha=0.5$.

4.4. Two regimes of the marangoni convection

The results of the parametric study of the Marangoni effect on the FP-driven convection are summarized in Fig. 7a, which presents the relationship between the maximum fluid velocity $|u|_{\rm max}$ computed at the free surface $(y=8\,$ mm) normalized by the characteristic velocity $v_{\rm c}$ and the Marangoni number Ma. As indicated by the definition introduced after (4), the Marangoni number depends on both T_0 and α_0 . The results shown in Fig. 7a point to two distinct regimes: first, $|u|_{\rm max}/v_{\rm c}$ increases with Ma until Ma reaches around 680 beyond which the trend reverses. This two-regime relationship also holds true for $|u|_{\rm max}$ at $y=4\,$ mm (middle line of the system) as shown in Fig. 7b. This regime transition was captured in the dependence of |u| on α_0 alluded to in Fig. 6.

The linear increase of $|u|_{\max}$ with Ma can be understood from a quasi-steady force balance between viscous and surface tension forces. More specifically, the force balance gives $(\mu|u|_{\max}/l_v)\,A_s\approx \left\lfloor\frac{\partial y}{\partial T}(T_{\rm f}-T_0)\right\rfloor w$, where l_v is the velocity gradient lengthscale, w is the depth into the page, and $A_{\rm s}\approx l_Tw$ is the area on which the stress acts. Here, l_T is the temperature gradient lengthscale over which $(T_{\rm f}-T_0)$ occurs. Re-arranging the expression for fluid velocity predicts $|u|_{\max}\approx \frac{1}{\mu}\frac{\partial y}{\partial T}(T_{\rm f}-T_0)(\frac{l_v}{l_T})$, and normalizing each side by $v_{\rm c}$ leads to $|u|_{\max}/v_{\rm c}\approx (\frac{l_v}{l_T})$ Ma according to the definition in Eq. (5). Not only does this expression predict the linear relationship observed for Ma < 680 in Fig. 7a, it also helps interpret the observed numerical front factor $(l_v/l_T\approx 60$ from Fig. 7) as the ratio of the velocity gradient lengthscale (by observation on the order of a few millimeters), to the temperature gradient lengthscale (by observation much smaller than a few millimeters); Fig. 5 is a good example comparing the gradients

of velocity and temperature. At higher Ma, this simple scaling is insufficient and the maximum velocity decreases due to more complex effects.

The emergence of the two regimes in the $|u|_{\text{max}}/v_{\text{c}}$ vs. Ma relationship is correlated to the competition between chemical (α) and temperature (T^*) convection. The competition is further highlighted in Fig. 8a, which presents typical 1-D profiles of α , T^* (left axis), and $|\mathbf{u}|$ (right axis) with $T_0 = 20$ °C and $\alpha_0 = 0.01$. The 1-D profiles were obtained on the free surface when t = 20 s. The profile of α (dashed pink curve) shows a sharp gradient associated with the cure kinetics of DCPD. Since the polymerization is thermally induced, the thermal profile (solid navy curve) precedes the chemical front. The profile of fluid velocity |u| (solid light blue curve) also precedes the front as it is driven by the thermal gradients (eq (4)). As expected, it rapidly vanishes behind the chemical front ($\alpha = 0.5$) due to the very sharp increase in the viscosity with the degree of cure. As highlighted in the inset of Fig. 8a, the non-zero fluid velocity |u| overlaps with the non-zero gradients of T^* and α , driving the advection of the chemical concentration (pink arrow) and temperature (navy arrow) in the positive x-direction, respectively.

Fig. 8b presents the 1-D profile of α and the Prandtl number Pr = v/D. The horizontal axis corresponds to the coordinate relative to the front location x_f normalized by the characteristic length l_c . A higher Ma promotes the advection of the degree of cure and hence leads to a higher value of Pr (viscosity), which in turn limits the fluid convection (Fig. 8c) and contributes to the second regime of $|u|_{max}/v_c$ described by Fig. 7. The x-location of the maximum velocity denoted by x_{max}^* on the normalized x-axis (x/l_c) in Fig. 8c progressively moves away from the front due to the increase in viscosity ahead of the front. A linear relationship between x_{max}^* and Ma is observed in Fig. 8d.

4.5. Effect of Marangoni convection on front propagation

To further shed insight on the effect of the surface tension driven convection on the propagation of the front, the evolution of the front location x_f (curves) and velocity v_f (symbols) with $\alpha_0 = 0.005$ and $T_0 = 20$ °C are shown in Fig. 9a. The velocity values were obtained by fitting the x_{f} -t data with a window of 0.2 s. The maximum value of v_f computed along the top surface (squares) is observed at t = 11s, which corresponds to the time at which the front reaches the free surface (Fig. 5a). As the heat of the thermal spike is progressively dissipated and the system enters the quasi-steady-state regime, v_f gradually reaches a stable value. In contrast to the upper boundary, v_f at the bottom boundary (circles) remains relatively constant at t = 11 s as it is not influenced by the thermal spike. Due to the convective motion of the fluid at the free surface, the v_f at the top boundary consistently exceeds that at the bottom boundary. As a result, the shape of the front undergoes continuous transformations, which aligns with the findings in Fig. 5. Similar conclusions can be drawn for monomer resins with an $\alpha_0 = 0.01$ and $T_0 = 20$ °C (Fig. S7q in the Supplementary Material).

During the stable period (e.g., from 25 to 35 s in Fig. 9a), it is feasible to calculate an average velocity $\overline{v_{\rm f}}$, which can be considered a characteristic of FP influenced by Marangoni convection. By varying the degree of cure (α_0) and keeping the initial temperature (T_0) constant at 20 °C, the average velocity ($\overline{v_{\rm f}}$) at the top and bottom can be compared (Fig. 9b). For all cases, the front velocity is always higher at the top boundary than the bottom boundary. Furthermore, it is worth noting that $\overline{v_{\rm f}}$ is substantially reduced as compared to the RD systems that lacks fluid convection (curve and triangles). The analytical expression of $\overline{v_{\rm f}}$ for the RD system is

$$\overline{v_{\rm f}} = \max_{\epsilon} \left[\frac{A\kappa}{\rho H_{\rm r}} \frac{R\hat{T}(\epsilon)^2}{E} \exp\left(\frac{-E}{R\hat{T}(\epsilon)}\right) \frac{1}{\Pi[n, \alpha_0, \epsilon]} \right]^{0.5}, \tag{8}$$

where $\hat{T}(\epsilon) = T_0 + \frac{(1-\alpha_0-\epsilon)H_{\rm r}}{C_p}$, ϵ is a small value between 0 and 1- α_0 , and $\Pi[n,\alpha_0,\epsilon] = \int_0^{1-\epsilon-\alpha_0} \frac{y}{(y+\epsilon)^n} \, dy$ is a coefficient related to the cure

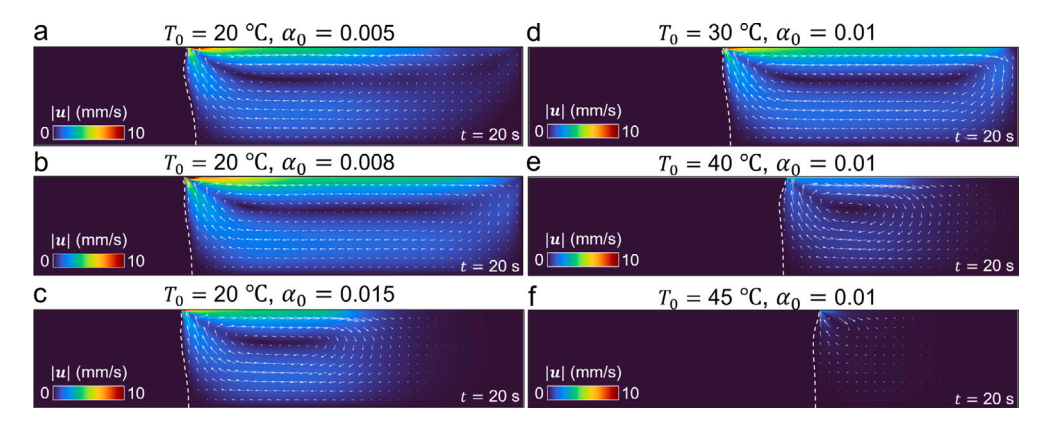


Fig. 6. Effect of process conditions (T_0 and α_0) on the fluid velocity magnitude field |u| obtained for t = 20 s. (a)–(c) $T_0 = 20$ °C and $\alpha_0 = 0.005$, 0.008, and 0.015. (d)–(f) $\alpha_0 = 0.01$ and $T_0 = 30$, 40, and 45 °C. The arrows indicate the local velocity vectors and the dashed lines correspond to the position of the front.

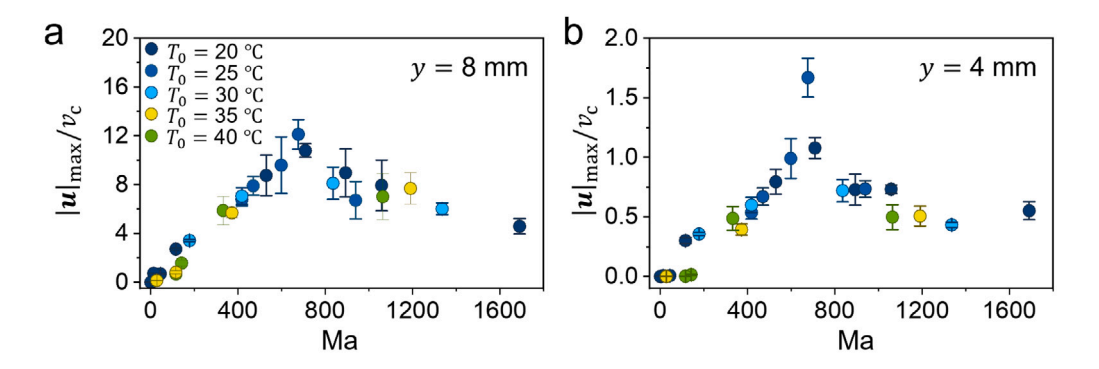


Fig. 7. Two regimes of the Marangoni convection during FP: Normalized maximum fluid velocity $|u|_{\text{max}}/v_{\text{c}}$ as a function of the Marangoni number Ma (a) at y=8 mm (at the free surface) and (b) 4 mm (along the middle horizontal line).

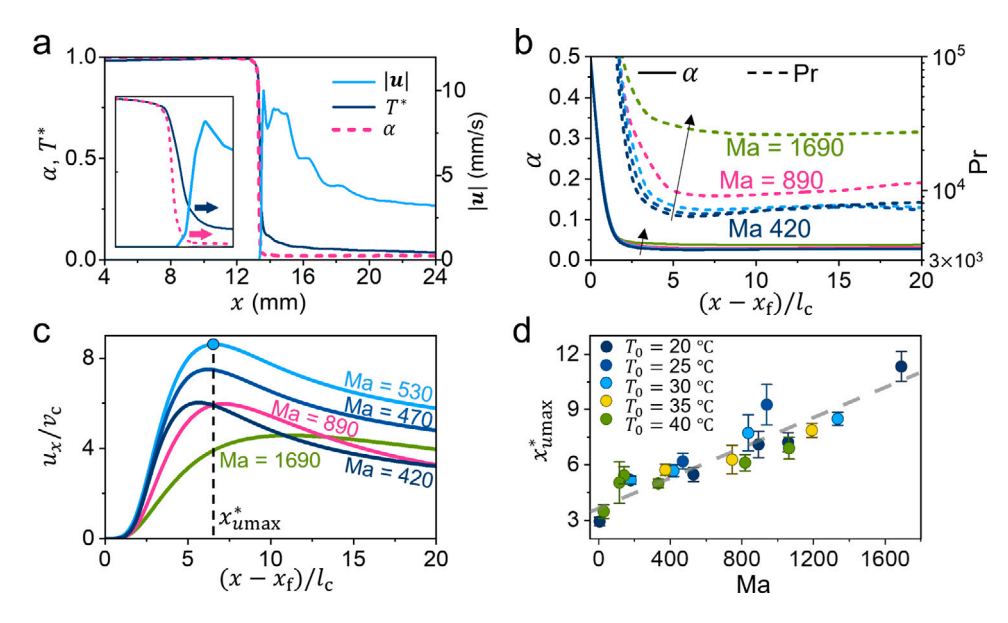


Fig. 8. Spatial variation of the solution near the polymerization front. (a) 1-D profiles of the degree of cure α_0 normalized temperature T^* , and fluid velocity magnitude |u| with the initial temperature $T_0 = 20$ °C and degree of cure $\alpha_0 = 0.01$. (b) Variation of α and the Prandtl number Pr ahead of the front, where x, x_t , and l_c denote the x-coordinate, front position, and characteristic length. (c) Variation of the normalized x-component of the fluid velocity factor u_x/v_c close to the front, where v_c is the characteristic velocity. The distance between the front and the location with maximum value of u_x is denoted by x^*_{mmax} on the normalized x-axis (x/l_c). (d) x^*_{mmax} as a function of the Marangoni number Ma.

kinetics parameter and the initial degree of cure (Kumar et al., 2021). The reduction of $\overline{v_f}$ for RDC systems is attributed to the dissipation of the heat from the reaction by the Marangoni convection. However, when the α_0 rises, leading to an increase in the monomer resin's viscosity, Marangoni convection becomes restricted, causing the front

velocity $\overline{v_{\mathrm{f}}}$ to converge to that of the corresponding RD systems. The correlation between $\overline{v_{\mathrm{f}}}$ and T_0 (circles and squares) is presented in Fig. 9c and compared with the RD theory and simulations (curve and triangles). Similarly, a higher T_0 reduces the fluid velocity, and $\overline{v_{\mathrm{f}}}$ values demonstrate a trend of approaching the RD theory.

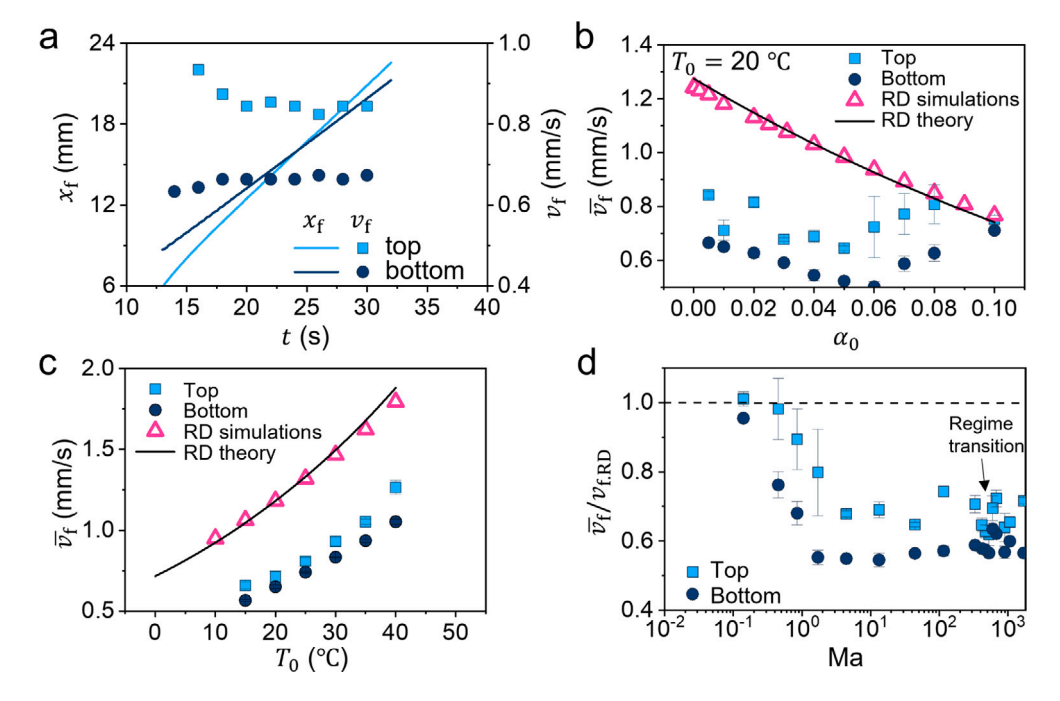


Fig. 9. Front propagation with Marangoni convection. (a) Front location x_f (curves) and velocity v_f (symbols) as a function of time t with $\alpha_0 = 0.005$ and $T_0 = 20$ °C. Averaged velocity $\overline{v_f}$ (squares and circles) during FP as a function of (b) the initial degree of cure α_0 , and (c) initial temperature (T_0). Numerical (triangles) and analytical (curve) front velocity values in the reaction–diffusion systems with the same α_0 and T_0 are displayed for comparison. (d) Normalized front velocity $\overline{v_f}/v_{f,RD}$ as a function of the Marangoni number Ma.

These findings can be summarized by a generalized relationship between $\overline{v_{\rm f}}$ normalized by the front velocity in RD systems $v_{\rm f,RD}$ and the Marangoni number, which characterizes the fluid convection (Fig. 9d). The significant reduction in $\overline{v_{\rm f}}/v_{\rm f,RD}$ from 1 (dashed line) to approximately 0.6 when Ma is less than 10^0 can be attributed to the dissipation of the heat by the fluid convection. At Ma \sim 680, $\overline{v_{\rm f}}$ values are found to oscillate around 0.7, which corresponds to the transition between the two regimes.

4.6. Instability and reaction patterns in FP induced by Marangoni convection

As mentioned in the previous section, an increase in the Marangoni convection (Ma > 680) can induce unstable front propagation. These unstable fronts can be visualized by extracting the evolution of the front location x_f (Fig. 10a). Two cases with $\alpha_0 = 0.01$ are illustrated: a stable FP with a linear x_f -t relationship at $T_0 = 40$ °C, and an unstable FP with an undulating $x_{\rm f}$ -t curve obtained for $T_0=10$ °C. The undulations reflect the periodic variation in v_f (slope of the x_f -t curve) driven by fluctuations in the reaction rates. The inset displays typical snapshots of the thermal solutions in the vicinity of the polymerization front for the two cases, clearly illustrating the presence of thermal heads in the unstable FP case. These thermal heads, referred to as 'spin modes' in previous studies (Masere et al., 1999), spin to the positive and negative y-direction, merge or sometimes separate (Video S1). The time evolution of the maximum reaction rate $\left(\partial\alpha/\partial t\right)_{max}$ in the stable and unstable FP cased is presented in Fig. 10b, showing much more pronounced fluctuations in the unstable case due to more significant convection effects.

The reaction patterns in stable and unstable FP with the 2-D distributions of $(\partial \alpha/\partial t)_{\rm max}$ at $10 \le x \le 20$ mm and $0 \le y \le 8$ mm, where the front propagation is in the quasi-steady-state regime, are visualized in Fig. 10c. In stable FP, the pattern is almost homogeneous (left panel), while a web-like pattern can be observed in the unstable FP case (right panel). The high-intensity regions in the pattern correspond to the positions of the thermal heads, while the lines that connect the high-intensity spots are the propagation paths of these thermal

heads. As shown in the inset, the web-like pattern is missing in the RD system (i.e., in the absence of convection) with the same FP processing conditions ($T_0 = 10$ °C and $\alpha_0 = 0.01$), clearly pointing to the critical role of convection on the FP-driven instabilities and reaction patterns.

The thermal patterns in stable and unstable FP are shown in Fig. 10d, which presents the distribution of the normalized maximum temperature $T_{\rm max}^* = (T_{\rm max} - T_0)/(T_{\rm f} - T_0)$. For stable FP, $T_{\rm max}^*$ is higher along the free surface since the fluid convection transfers heat from the bottom to the top boundary. The $T_{\rm max}^*$ solution is uniform in the x direction, with no discernible patterns, as opposed to the unstable FP case, for which high-intensity 'thermal spots' are observed, which coincide with the reaction pattern.

The features of the reaction patterns can be adjusted by modifying the processing conditions (T_0 and α_0), as illustrated in Fig. 11a,b. With a fixed $\alpha_0=0.01$, the wavelength of the pattern λ , defined as the average distance between high-intensity spots at the free surface, is decreases as T_0 increases. The reaction patterns also become less visible at higher values of T_0 suggesting a lower degree of instability. This result is similar to thermo-chemical instabilities capture by the reaction-diffusion model (i.e., in the absence of fluid convection) and can be attributed changes in the balance between reaction and diffusion (Goli et al., 2020; Lloyd et al., 2021). Similarly, the patterns are also less pronounced as α_0 increases at a fixed value of the initiation temperature ($T_0=20~{\rm ^{\circ}C}$) as shown in Fig. 11b.

To characterize the degree of instability, a reaction-rate ratio η_a is defined as the maximum reaction rate of the instability peaks normalized by the average value over the entire domain. The relationships between η_a and the processing conditions (T_0 and α_0) demonstrate nonmonotonic trends as observed in Fig. 11c. In both correlations, the turning point corresponds to Ma \sim 680, which is associated with the maximum normalized fluid velocity $|u|_{\rm max}/v_c$ and the regime transition (Fig. 7). This finding can be confirmed by the relationship between η_a and Ma shown in the inset. Moreover, these observations suggest that the fluid convection disturbs the reaction–diffusion balance and triggers the instability, with the extent of instability amplified by the magnitude of the fluid velocity. The effect of T_0 and α_0 on the wavelength λ is presented in Fig. 11d. Unlike for η_a , no generalized

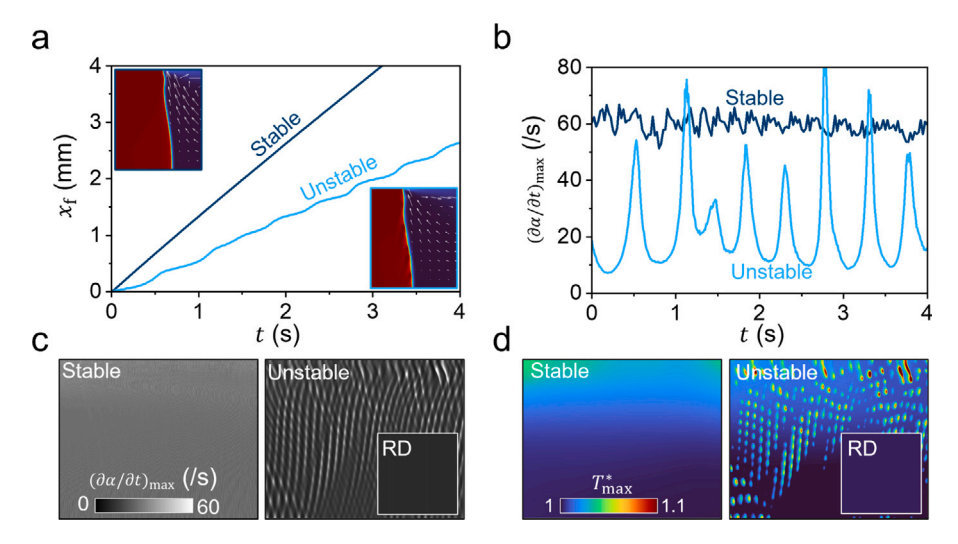


Fig. 10. Stable and unstable FP with Marangoni convection. (a) Front location $x_{\rm f}$ as a function of time t in stable (dark blue) and unstable (light blue) FP. Insets display typical thermal solutions in the vicinity of the front. (b) Evolution of the maximum reaction rate in the system $(\partial a/\partial t)_{\rm max}$ in stable and unstable FP. Reaction (c) and thermal patterns (d) in stable and unstable FP represented by the distributions of maximum reaction rate $(\partial a/\partial t)_{\rm max}$ and normalized temperature $T_{\rm max}^*$, respectively. Insets: no patterns are observed in the reaction–diffusion systems under the same initial conditions (α_0, T_0). (For interpretation of the references to color in this figure legend, the reader is referred to the web version of this article.)

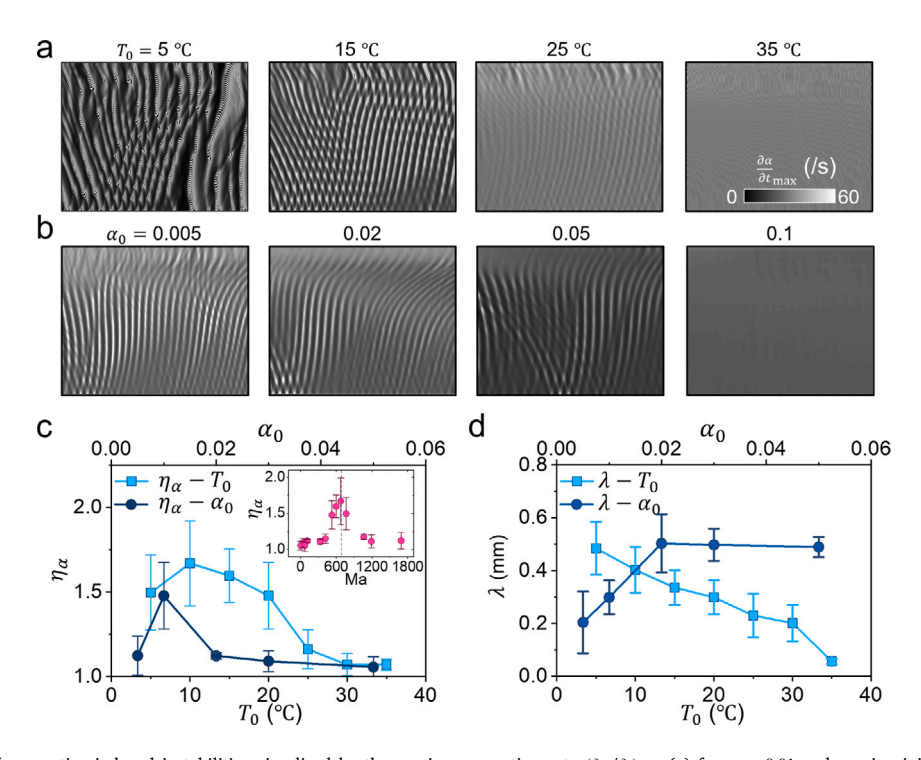


Fig. 11. Reaction patterns of convection-induced instabilities visualized by the maximum reaction rate $(\partial \alpha/\partial t)_{\rm max}$ (a) for $\alpha_0=0.01$ and varying initial temperature T_0 and (b) at $T_0=20$ °C and four α_0 values. (c) Reaction-rate ratio η_α , defined as the maximum reaction rates of the instability peaks normalized by the average value over the whole domain, as functions of α_0 and T_0 . (d) Wavelength λ of the pattern, defined as the average distance between high-intensity reaction-rate peaks measured at the free surface, as functions of α_0 and T_0 .

relationship between λ and Ma can be established, which indicates the fluid convection is not the only factor that influences λ .

4.7. FP experiments in an open mold with particle image velocimetry

Free-surface frontal polymerization experiments on the 70/30 DCPD/ENB system coupled with PIV have been conducted to support and validate the numerical results presented above. The addition of ENB is necessary to ensure experiments are within the quasi-static front propagation regime at various processing parameters (T_0 and α_0) for \sim 20 s. A schematic of the experimental setup is presented in Fig. 12a.

A representative optical image captured during the polymerization process is shown in Fig. 12b where the approximate location of the propagating front is marked by the yellow dashed curve. The corresponding distribution of the flow field |u| obtained by post-processing adjacent frames is presented in Fig. 12c. The black arrows indicate the orientation of the local fluid velocity vectors and point to a convective vortex in the clockwise direction. An optical video of the FP experiment with $a_0=0.01$ and $T_0=30~{\rm ^{\circ}C}$ is provided in the Supplementary Material (Video S2). An additional optical video without the laser sheet reveals the fluid-induced instability (Video S3).

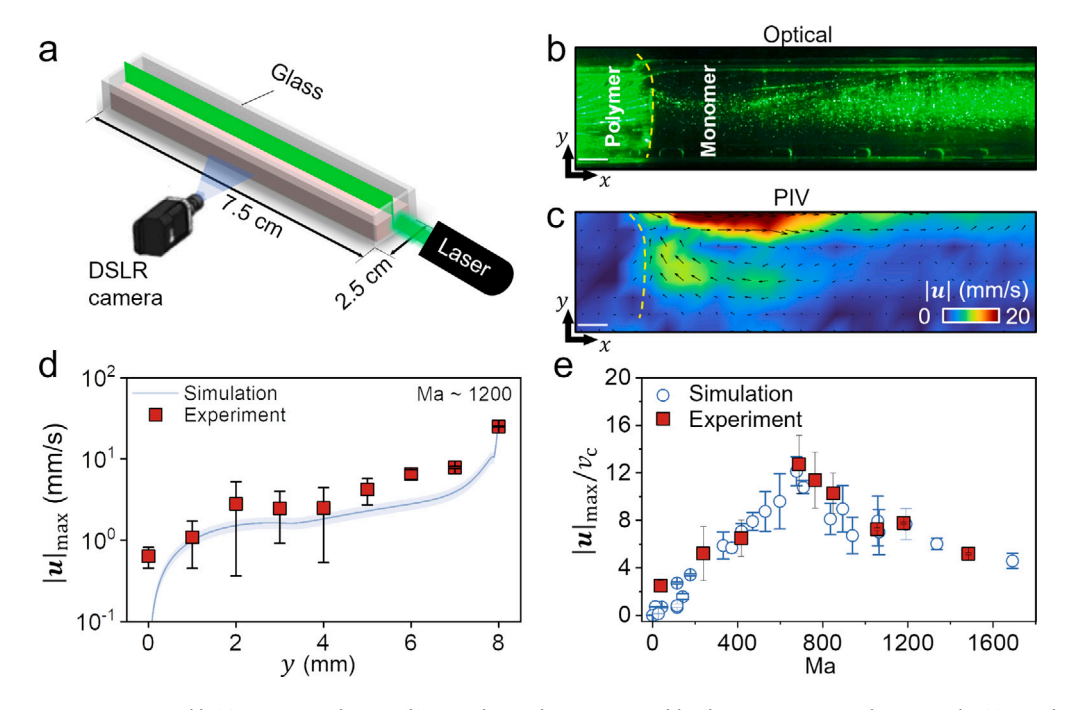


Fig. 12. PIV FP experiments in an open mold. (a) Experimental setup. (b) Typical optical image captured by the DSLR camera in the gray scale. (c) Distribution of fluid velocity magnitude |u| corresponding to (b). Scale bars indicate 2 mm. (d) $|u|_{max}$ vs. y: comparison between numerical results (curve) and experimental measurements (symbols) for a Marangoni number Ma \sim 1200. (e) Normalized maximum fluid velocity magnitude $|u|_{max}/v_c$ as a function of Ma obtained numerically (circles) and experimentally (squares).

The Marangoni number can be estimated for the experiments by measuring the heat of reaction (H_r) , viscosity (μ) , and degree of cure (α_0) of the monomer resin along with programming the ambient temperature (T_0) using an environmental chamber. The heat of reaction H_r for the monomer resin system with 100 ppm of catalyst and 1 equivalent of inhibitor to catalyst is 402.5 J/g and the degree of cure (α_0) measured immediately after mixing all the resin components together is roughly 0.005. These experimental values can be tuned by incubating the monomer at a constant temperature for a specified period of time (Robertson et al., 2018; Aw et al., 2022; Garg et al., 2021). Post-processing the simulation and experimental results corresponding to Ma \sim 1200 allows for a direct comparison of the maximum magnitude of the fluid velocity ($|u|_{max}$) at various locations along the yaxis. The results presented in Fig. 12d show a good agreement between simulations and experiments, and confirms that the maximum fluid velocity is at the free surface (y = 8 mm) right ahead of the front. The laser was unable to fully illuminate the sample due to light reflection and refraction at material interfaces, and the region of y < 4 mm is typically darker, which contributes to the more significant uncertainty compared to other regions (Fig. 12b).

By varying the experimental processing conditions, a range of Marangoni numbers can be achieved. A comparison between numerical predictions and experimental measurements of the dependence of the normalized maximum fluid velocity magnitude $|\mathbf{u}|_{\rm max}/v_{\rm c}$ on the Marangoni number is presented in Fig. 12e, showing again an excellent agreement in capturing the two regimes alluded to in Fig. 7. The agreement is non-trivial considering the complex thermo-chemical advection with finite fluid inertia, e.g., an estimate of Reynolds number for the experiments in Fig. 12c gives Re ≈ 40 (using characteristic speed 20 mm/s, lengthscale 2 mm, and the uncured viscosity to get an upper-bound estimate), indicating the need for inertial terms on the left side of Eq. $(1)_4$. These results further validate the competition between thermal advection and chemical concentration at Marangoni numbers above 680. The value and uncertainties in numerical and experimental results have been obtained by averaging 400 simulation frames and 40 optical images within the quasi-steady-state regime of front propagation, respectively.

5. Conclusions

We have investigated numerically and experimentally the fluid convection that arises during the frontal polymerization of dicyclopentadiene in a free-surface (open mold) geometry. Prior to the interaction of the polymerization front with the free surface, the dimensionless frontal Rayleigh number dictates the fluid convection induced by buoyancy effects. After the front reaches the free surface of the liquid resin, the amplitude of the fluid convection driven by the surface tension gradient, referred to as the Marangoni convection, is found to be two orders of magnitude higher than that of the buoyancyinduced convection. A detailed parametric study has shown that the magnitude of the fluid velocity in the Marangoni convection regime depends on the processing conditions, including the initial temperature and the degree of cure. The effects of the processing conditions can be summarized by the non-monotonic trend between the maximum amplitude of the fluid velocity and the dimensionless Marangoni number, Ma. This non-monotonic dependence on Ma can be attributed to the competition between the thermal advection associated with the fluid motion and the rapid increase of viscosity due to the curing process. At Marangoni numbers in excess of about 680, the strong fluid momentum can induce unstable front propagation and lead to the generation of reaction patterns, the wavelength and magnitude of which can be adjusted by the initial temperature and degree of cure. These numerical findings are validated by FP experiments performed on an open-mold DCPD resin, with details on the convective flow captured using particle image velocimetry. Experimental and numerical results show a very good agreement. This work demonstrates a quantitative understanding of the Marangoni flow and the processing conditions of frontal polymerization, providing theoretical guidance for harnessing the fluid flow in FP-based manufacturing process with a free surface.

CRediT authorship contribution statement

Yuan Gao: Formal analysis, Investigation, Writing – original draft, Writing – review & editing. Justine E. Paul: Writing – review & editing, Investigation, Formal analysis, Methodology, Writing – original draft. Manxin Chen: Software, Formal analysis, Data curation. Aarav Seth:

Formal analysis. Qibang Liu: Data curation, Formal analysis, Methodology. Liu Hong: Methodology. Leonardo P. Chamorro: Writing – review & editing, Writing – original draft, Methodology, Resources, Supervision. Randy H. Ewoldt: Writing – review & editing, Writing – original draft, Methodology, Conceptualization. Nancy R. Sottos: Writing – review & editing, Funding acquisition, Conceptualization, Project administration, Resources, Supervision, Writing – original draft. Philippe H. Geubelle: Writing – review & editing, Conceptualization, Funding acquisition, Project administration, Resources, Supervision, Writing – original draft.

Declaration of competing interest

The authors declare that they have no known competing financial interests or personal relationships that could have appeared to influence the work reported in this paper.

Data availability

Data will be made available on request.

Acknowledgments

This work was supported by the U.S. Air Force Office of Scientific Research through Award FA9550-20-1-0194 as part of the Center of Excellence in Self-healing and Morphogenic Manufacturing. The authors also acknowledge the support of the National Science Foundation, United States for Grant No. 1933932 through the GOALI: Manufacturing USA: Energy Efficient Processing of Thermosetting Polymers and Composites.

Appendix A. Supplementary data

Supplementary material related to this article can be found online at https://doi.org/10.1016/j.mechmat.2024.104987.

References

- Aw, J.E., Zhang, X., Nelson, A.Z., Dean, L.M., Yourdkhani, M., Ewoldt, R.H., Geubelle, P.H., Sottos, N.R., 2022. Self-regulative direct ink writing of frontally polymerizing thermoset polymers. Adv. Mater. Technol. 2200230.
- Bába, P., Rongy, L., De Wit, A., Hauser, M., Tóth, Á., Horváth, D., 2018. Interaction of pure marangoni convection with a propagating reactive interface under microgravity. Phys. Rev. Lett. 121 (2), 024501.
- Bazile, Jr., M., Nichols, H.A., Pojman, J.A., Volpert, V., 2002. Effect of orientation on thermoset frontal polymerization. J. Polym. Sci. A Polym. Chem. 40 (20), 3504–3508
- Belk, M., Kostarev, K.G., Volpert, V., Yudina, T.M., 2003. Frontal photopolymerization with convection. J. Phys. Chem. B 107 (37), 10292–10298.
- Bigaj, A., Budroni, M.A., Escala, D.M., Rongy, L., 2023. Marangoni-vs. buoyancy-driven flows: competition for spatio-temporal oscillations in A+ B→ C systems. Phys. Chem. Chem. Phys. 25 (16), 11707–11716.
- Bowden, G., Garbey, M., Ilyashenko, V.M., Pojman, J.A., Solovyov, S.E., Taik, A., Volpert, V.A., 1997. Effect of convection on a propagating front with a solid product: comparison of theory and experiments. J. Phys. Chem. B 101 (4), 678–686.
- Chechilo, N., Khvilivitskii, R., Enikolopyan, N., 1972. Propagation of the polymerization reaction. In: Dokl. Akad. Nauk SSSR, Vol. 204, pp. 1180-1181.
- Chen, S., Tian, Y., Chen, L., Hu, T., 2006. Epoxy resin/polyurethane hybrid networks synthesized by frontal polymerization. Chem. Mater. 18 (8), 2159–2163.
- Chen, Z., Ziaee, M., Yourdkhani, M., Zhang, X., 2022. Multiphysics modeling of frontal polymerization-assisted layer-by-layer additive manufacturing of thermoset polymer components. Addit. Manuf. 59, 103182.
- Davtyan, S., Berlin, A., Tonoyan, A., 2011. Advances and problems of frontal polymerization processes. Rev. J. Chem. 1 (1), 56–92.
- Gao, Y., Dearborn, M.A., Vyas, S., Kumar, A., Hemmer, J., Wang, Z., Wu, Q., Alshangiti, O., Moore, J.S., Esser-Kahn, A.P., et al., 2021. Manipulating frontal polymerization and instabilities with phase-changing microparticles. J. Phys. Chem. B 125 (27), 7537–7545.
- Gao, Y., Li, S., Kim, J.-Y., Hoffman, I., Vyas, S.K., Pojman, J.A., Geubelle, P.H., 2022a. Anisotropic frontal polymerization in a model resin-copper composite. Chaos 32 (1), 013109.

- Gao, Y., Paul, J., Chen, M., Hong, L., Chamorro, L., Sottos, N., Geubelle, P., 2023. Buoyancy-induced convection driven by frontal polymerization. Phys. Rev. Lett. 130 (2), 028101.
- Gao, Y., Rodriguez Koett, L.E., Hemmer, J., Gai, T., Parikh, N., Sottos, N.R., Geubelle, P.H., 2022b. Frontal polymerization of thin layers on a thermally insulating substrate. ACS Appl. Polym. Mater. 4 (10), 6880–6886.
- Garbey, M., Taik, A., Volpert, V., 1996. Linear stability analysis of reaction fronts in liquids. Q. Appl. Math. 54 (2), 225–247.
- Garg, M., Aw, J.E., Zhang, X., Centellas, P.J., Dean, L.M., Lloyd, E.M., Robertson, I.D., Liu, Y., Yourdkhani, M., Moore, J.S., et al., 2021. Rapid synchronized fabrication of vascularized thermosets and composites. Nature Commun. 12 (1), 2836.
- Gaston, D., Newman, C., Hansen, G., Lebrun-Grandie, D., 2009. MOOSE: a parallel computational framework for coupled systems of nonlinear equations. Nucl. Eng. Des. 239 (10), 1768–1778.
- Goli, E., Peterson, S.R., Geubelle, P.H., 2020. Instabilities driven by frontal polymerization in thermosetting polymers and composites. Composites B 199, 108306.
- Goli, E., Robertson, I.D., Geubelle, P.H., Moore, J.S., 2018. Frontal polymerization of dicyclopentadiene: a numerical study. J. Phys. Chem. B 122 (16), 4583–4591.
- Ivanoff, D.G., Sung, J., Butikofer, S.M., Moore, J.S., Sottos, N.R., 2020. Cross-linking agents for enhanced performance of thermosets prepared via frontal ring-opening metathesis polymerization. Macromolecules 53 (19), 8360–8366.
- Koohbor, B., Zhang, X., Dean, L., Yourdkhani, M., Geubelle, P., Sottos, N., 2023. Experimental characterization and multiphysics modeling of residual deformation in manufacturing of thermosetting polymers by frontal polymerization.
- Kumar, A., Gao, Y., Geubelle, P.H., 2021. Analytical estimates of front velocity in the frontal polymerization of thermoset polymers and composites. J. Polym. Sci. 59 (11), 1109–1118.
- Kumar, A., Zakoworotny, M., Bonner, F.J.B., Aw, J.E., Sottos, N.R., Tawfick, S.H., Geubelle, P.H., 2024. A thermo-chemo-mechanical model for material extrusion of frontally polymerizing thermoset polymers. Addit. Manuf. 103972.
- Li, Q., Shen, H.-X., Liu, C., Wang, C.-f., Zhu, L., Chen, S., 2022. Advances in frontal polymerization strategy: From fundamentals to applications. Prog. Polym. Sci. 101514.
- Liu, Y., Ren, X., Pan, C., Zheng, T., Yuan, L., Zheng, J., Gao, Q., 2017. Chlorine dioxide-induced and congo red-inhibited marangoni effect on the chlorite-trithionate reaction front. Chaos 27 (10).
- Lloyd, E.M., Feinberg, E.C., Gao, Y., Peterson, S.R., Soman, B., Hemmer, J., Dean, L.M., Wu, Q., Geubelle, P.H., Sottos, N.R., et al., 2021. Spontaneous patterning during frontal polymerization. ACS Cent. Sci. 7 (4), 603–612.
- Mariani, A., Bidali, S., Fiori, S., Sangermano, M., Malucelli, G., Bongiovanni, R., Priola, A., 2004. UV-ignited frontal polymerization of an epoxy resin. J. Polym. Sci. A Polym. Chem. 42 (9), 2066–2072.
- Mariani, A., Fiori, S., Chekanov, Y., Pojman, J.A., 2001. Frontal ring-opening metathesis polymerization of dicyclopentadiene. Macromolecules 34 (19), 6539–6541.
- Masere, J., Stewart, F., Meehan, T., Pojman, J.A., 1999. Period-doubling behavior in frontal polymerization of multifunctional acrylates. Chaos 9 (2), 315–322.
- Matthiessen, K., Wilke, H., Müller, S.C., 1996. Influence of surface tension changes on hydrodynamic flow induced by traveling chemical waves. Phys. Rev. E 53 (6), 6056.
- McCaughey, B., Pojman, J.A., Simmons, C., Volpert, V., 1998. The effect of convection on a propagating front with a liquid product: comparison of theory and experiments. Chaos 8 (2), 520–529.
- Mukherjee, S., Paul, M., 2022. The fluid dynamics of propagating fronts with solutal and thermal coupling. J. Fluid Mech. 942, A36.
- Nason, C., Roper, T., Hoyle, C., Pojman, J.A., 2005. UV-induced frontal polymerization of multifunctional (meth) acrylates. Macromolecules 38 (13), 5506–5512.
- Nuvoli, D., Alzari, V., Pojman, J.A., Sanna, V., Ruiu, A., Sanna, D., Malucelli, G., Mariani, A., 2015. Synthesis and characterization of functionally gradient materials obtained by frontal polymerization. ACS Appl. Mater. Interfaces 7 (6), 3600–3606.
- Pojman, J.A., 2019. Mathematical modeling of frontal polymerization. Math. Modell. Nat. Phenom. 14 (6), 604.
- Pojman, J.A., Ilyashenko, V.M., Khan, A.M., 1996. Free-radical frontal polymerization: self-propagating thermal reaction waves. J. Chem. Soc. Faraday 92 (16), 2825–2837.
- Robertson, I.D., Pruitt, E.L., Moore, J.S., 2016. Frontal ring-opening metathesis polymerization of exo-dicyclopentadiene for low catalyst loadings. ACS Macro Lett. 5 (5), 593–596.
- Robertson, I.D., Yourdkhani, M., Centellas, P.J., Aw, J.E., Ivanoff, D.G., Goli, E., Lloyd, E.M., Dean, L.M., Sottos, N.R., Geubelle, P.H., et al., 2018. Rapid energyefficient manufacturing of polymers and composites via frontal polymerization. Nature 557 (7704), 223–227.
- Ruiu, A., Sanna, D., Alzari, V., Nuvoli, D., Mariani, A., 2014. Advances in the frontal ring opening metathesis polymerization of dicyclopentadiene. J. Polym. Sci. A Polym. Chem. 52 (19), 2776–2780.
- Suslick, B.A., Hemmer, J., Groce, B.R., Stawiasz, K.J., Geubelle, P.H., Malucelli, G., Mariani, A., Moore, J.S., Pojman, J.A., Sottos, N.R., 2023. Frontal polymerizations: from chemical perspectives to macroscopic properties and applications. Chem. Rev. 123 (6), 3237–3298.

- Suslick, B.A., Stawiasz, K.J., Paul, J.E., Sottos, N.R., Moore, J.S., 2021. Survey of catalysts for frontal ring-opening metathesis polymerization. Macromolecules 54 (11), 5117–5123.
- Tarafdar, A., Jia, C., Hu, W., Hosein, I.D., Fu, K.K., Wang, Y., 2023. Three-dimensional modeling of frontal polymerization for rapid, efficient, and uniform thermoset composites manufacturing. Composites B 266, 111029.
- Tiani, R., De Wit, A., Rongy, L., 2018. Surface tension-and buoyancy-driven flows across horizontally propagating chemical fronts. Adv. Colloid Interface Sci. 255, 76–83.
- Tiani, R., Pojman, J.A., Rongy, L., 2022. Critical role of layer thickness in frontal polymerization. J. Phys. Chem. B 126 (19), 3607–3618.
- Vyas, S., Goli, E., Zhang, X., Geubelle, P., 2019. Manufacturing of unidirectional glass-fiber-reinforced composites via frontal polymerization: A numerical study. Compos. Sci. Technol. 184, 107832.
- Vyas, S., Zhang, X., Goli, E., Geubelle, P., 2020. Frontal vs. bulk polymerization of fiber-reinforced polymer-matrix composites. Compos. Sci. Technol. 198, 108303.
- Wang, Y., 2022. Modeling the through-thickness frontal polymerization of unidirectional carbon fiber thermoset composites: Effect of microstructures. J. Appl. Polym. Sci. 139 (31), e52735.
- Washington, R.P., Steinbock, O., 2001. Frontal polymerization synthesis of temperature-sensitive hydrogels. J. Am. Chem. Soc. 123 (32), 7933–7934.